Nanobridge Stencil Enabling High Resolution Arbitrarily Shaped Metallic Thin Films on Various Substrates

Yi-Chiang Sun,* Giovanni Boero, and Jürgen Brugger*

Stencil lithography (SL), which uses a perforated membrane as a reusable shadow mask to locally add material patterns on substrates provides a simple but versatile approach for the fabrication of functional devices on a large variety of substrate materials by physical vapor deposition (PVD). Mechanical stress induced by the accumulation of condensed material on the thin stencil membrane during the PVD step leads to stencil bending and breaking, therefore, suspended stencil membranes with arbitrary openings are, in practice, not possible. Here, a new approach to remedy this limitation is reported by introducing auxiliary bridges in stencils. These bridges prevent the suspended membrane from bending out of plane, thereby enabling aperture openings to have almost arbitrary geometry. These bridges are sufficiently narrow so that they do not entirely block the material deposition by PVD and thus create a continuous material pattern by taking advantage of the blurring effect. The successful metal deposition through the designed nanobridge stencil on a wide range of substrate materials underlines the usability and the versatility of the proposed stencil design. The work presented here provides a versatile fabrication method to produce arbitrarily shaped metal patterns that were previously impossible due to the topological constraints of nanostencils.

1. Introduction

Realizing functional devices on polymer substrates has enabled a wide range of applications such as artificial skin,[1] skin-integrated haptic interfaces,[2] biomedical,[3] and implantable sensors.[4] Conventional resist-based processes involve the use of harsh chemicals to define patterns, which make them not suitable for polymer substrate materials because most of polymers are vulnerable to acidic or basic solutions. Recently, non-conventional fabrication processes which avoid exposure to harsh chemicals have been widely studied to realize wearable and implantable devices. For instance, the demonstration of

transfer printing of devices prefabricated on a rigid substrate to a polymer substrate represented an important milestone in flexible and stretchable devices[5,6] and bio-degradable electronics.[7] Since the devices are prefabricated on a rigid substrate (e.g., Si), transfer printing allows the use of a wide range of materials and well-established semiconductor processes to realize high performance electronic devices on various substrate materials. For example, stretchable strain and temperature sensors based on single crystalline Si were monolithically integrated on a stretchable PDMS substrate by transferring the prefabricated devices onto the substrate for epidermal electronic applications.[8] The advances in the stamp design enabled the realization of functional devices on arbitrary 3D substrates.[9,10] However, despite several remarkable achievements in the transfer printing technique, realizing sub-micrometer or nanometer scale structures by utilizing this technique remains challenging.

An alternative approach to transfer printing consists of the use of a shadow mask technique (i.e., stencil lithography (SL)) to directly fabricate the designed structures on substrates.[11] It provides the ability to produce high-resolution patterns without the need for series processes such as resist coating and developing. The working principle of SL is based on the use of a free-standing membrane with opening apertures to locally deposit or etch materials. In contrast to the transfer printing technique, it provides a clean and cost-efficient way to directly fabricate devices on the target substrate, while maintaining high resolution down to the nanometer scale. SL is reusable, and due to its resistless characteristic, it has been utilized for a variety of applications including stretchable[12] and biodegradable electronics.[13] In addition, SL was used to fabricate electrical contacts on 2D materials for its documented lower impact on the material properties when compared to electron beam lithography (EBL).[14]

Rigid, and chemically resistant stencils are commonly fabricated using silicon nitride (SiN) as membrane material. SiN is broadly used in semiconductor processes because it can be grown by chemical vapor deposition (CVD). The stress of the grown SiN film can be adjusted by modulating CVD parameters such as deposition temperature and the ratio between the used precursors, which enables a low stress SiN (LS-SiN) film, an excellent candidate material for stencil applications. Utilizing SiN stencils with apertures patterned by EBL, sub-100

Y.-C. Sun, G. Boero, J. Brugger
Microsystems Laboratory
École Polytechnique Fédérale de Lausanne (EPFL)
Lausanne CH-1015, Switzerland
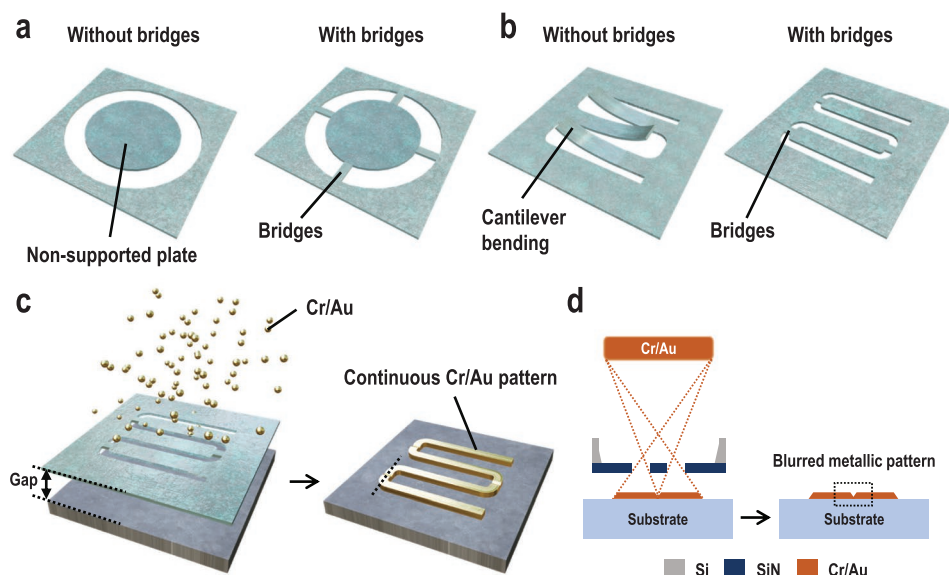E-mail: yi-chiang.sun@epfl.ch; juergen.brugger@epfl.ch

Figure 1. The concept of bridge stencils and the blurring effect. a,b) Schematic drawings showing the use of bridges for a) realizing unfeasible geometries on stencils (e.g., close-loop circular apertures), and b) suppressing the bending of cantilevers for meandering apertures. c,d) Schematic drawing showing the beneficial use of the blurring effect. When the stencil is lifted at an appropriate gap distance above the substrate, the blurring effect resulting from the line-of-sight evaporation process causes material deposition under the shadowed bridge region. The black dashed lines indicate where the cross-section profiles are extracted.

nm structures were realized on polymer substrates for plasmonic biosensing.[15,16] Since suspended SiN membranes are supported by a thick Si frame, SiN stencils present the capability of full wafer patterning. The easy-to-handle SiN stencil enables structuring nanometer features at the full wafer scale as well as the ability to fine-pitch alignment.[17,18]

In the conventional approach to the design of stencils, the apertures in the membrane cannot have an arbitrary geometry. For example, close-loop apertures (e.g., O shapes) in stencils are practically not possible due to the lack of supports in the remaining membrane structures (**Figure 1**a). Applying SL in a dynamic mode where the stencil moves with respect to the substrate during the deposition process allowed the production of close-loop patterns.[19,20] However, dynamic SL leads to a huge waste of materials, making it not cost-efficient. In addition, the residual stress built up during the stencil fabrication process results in membrane bending after it is released from the Si substrate (Figure 1b). The membrane bending results in an inaccurate pattern definition of the material deposited on the substrate. Therefore, structures such as meanders and long slits aiming for an accurate pattern definition using SL are practically not possible. These challenges constrain the geometrical design flexibility of SL and set a limit on potential applications. Strategies applied to solve these challenges focused on increasing the cross sectional moment of inertia of stencil membranes by incorporating additional Si supports[21,22] or introducing corrugations.[23,24] However, the reported methods require additional fabrication steps and relatively complicated patterns such as spiral and meandering patterns have not been demonstrated yet. Another strategy involves the use of bridges to connect isolated islands to enable doughnut-shape-like apertures on stencil membranes. Using bridges having a

width in the range from 5 to 35 µm, various close-loop metallic structures were realized on Si substrates.[25]

Another particular feature of SiN stencils is the inherent gap existing between the stencil mask and the substrate. The gap results from the wafer curvature, stress induced bending of the stencil membrane and the substrate topography. Compared to conventional resist-based processes, where a photoresist is adhered to the substrate, the inherent gap in SL allows producing structures on fragile substrates that could be damaged by resist-based processes due to UV radiation, energetic electrons, or mechanical contact. However, the gap results in pattern enlargement of the deposited structures, an effect commonly called blurring. The blurring effect is due to the geometrical trajectory of the incoming atoms (geometrical blurring) and the surface diffusion of the deposited atoms (halo blurring).[26] The geometrical blurring has been thoroughly studied and can be approximately estimated by considering the aperture size, the stencil/substrate gap, the substrate/source distance, and the source size.[26] The halo blurring length is affected by the differences in the diffusion constant among different materials.[27] Although the blurring effect leads to a typically undesired pattern enlargement (i.e., limits the pattern resolution), it was utilized to control the crystallization of organic thin films through the surface diffusion of absorbed molecules,[28] and also to form continuous films with a well-controlled grain size.[29]

Here, we report on the extended use of bridges to overcome the limitation of geometrical design flexibility of stencils to realize high resolution arbitrarily shaped metallic patterns on a variety of polymer substrate materials. Compared to the previous literature,[25] we demonstrate the use of narrower bridges (1 µm and 250 nm) to enable high resolution metallic patterns.

Additionally, we study the use of bridge stencils not only on biocompatible but also on biodegradable polymer substrates, enabling devices for wearable and implantable applications. The bridge stencils presented here utilize uniformly distributed bridges on stencils to stabilize the freestanding membranes, thereby enabling a variety of aperture openings (Figure 1a,b). The suspended membrane is bounded to remain in the same plane as the surrounding membrane by narrow bridges. The applied narrow bridges allow not only the realization of conventionally unfeasible geometries on stencils (e.g., close-loop apertures; Figure 1a), but also the suppression of membrane bending for meandering apertures (Figure 1b). The blurring effect, which has long been a disadvantage in SL is converted into a solution for creating continuous material traces. By lifting the stencil at an appropriate gap distance above the substrate, the enhanced blurring effect leads to the material deposition under the shadowed bridge region (Figure 1c). Due to the line-of-sight evaporation process, high resolution patterns can be produced by properly designing the gap distance between the stencil and the substrate (Figure 1d). As demonstrative examples, we fabricated continuous spiral structures at the micrometer scale and meandering structures at the sub-micrometer scale on both rigid and soft substrate materials. The geometrical and electrical characterizations demonstrate the success of applying bridge stencils for direct fabrication of functional metal structures on a variety of substrate materials, an important step toward the use of this approach for the fabrication of soft and implantable devices with resolution down to sub-micrometer range.

2. Results and Discussion

In the following we report and discuss the results of experiments performed to demonstrate the key features of the proposed bridge stencil approach. The experiments have been performed with stencils having features down to 1 µm (microbridge stencil) and down to 250 nm (nanobridge stencil). The fabrication of the stencils is described in the Experimental Section.

2.1. Microbridge Stencil

We begin by investigating the effects of applying narrow bridges as a countermeasure to the stress built up on stencil membranes using a cantilever as a proof structure. The stencil mask used here consists of freestanding 500 nm-thick LS-SiN membranes supported by a Si frame. The fabrication starts from defining apertures on the front side LS-SiN, followed by back side etching of the Si to release the membrane. We fabricate on stencils several cantilevers having a width of 15 µm and lengths ranging from 50 to 900 µm with and without microbridges (**Figure 2**a). The 1 µm wide microbridges are placed at different interdistances ranging from 25 to 900 µm (i.e., D shown in Figure 2a). To gain quantitative understanding of the efficacy of the bridge placement, we characterize the accuracy of the resulting patterns transferred through the u-shape apertures of cantilever stencils. The stencils are first placed in contact with a Si substrate, fol-

lowed by evaporation deposition of 25 nm Cr. Here, Cr is selected to enhance bending of cantilevers during metal deposition because it is known to have a high thin film stress. In the experiment, the thin film stress of the deposited 25 nm Cr is about 3000 MPa, which is calculated by measuring the wafer curvature before and after metal deposition on a reference wafer. After Cr deposition and removal of the stencil, 60 nm of Si is etched by reactive ion etching using the deposited Cr as a mask to enhance the contrast of the resulting structures. As expected, using the stencil without bridges, we observe inaccurate pattern transfer of some membrane apertures, especially with longer cantilevers (Figure 2b). To quantify the accuracy of the transferred patterns, we define a parameter α, which is the length of the unwanted Cr structures deposited on the substrate due to the bending of the cantilevers (Figure S2, Supporting Information). The SEM and confocal images indicate significant bending of the cantilevers after the deposition of a 25 nm thick Cr layer (Figure 2c,d). For example, bending of around 50 µm is observed on the 150 µm long cantilever. On the other hand, with the stencil with microbridges, α is significantly reduced (Figure 2e). For instance, on the cantilever having a width of 15 µm and a length of 900 µm, microbridges with an interdistance (i.e., D in Figure 2a) of 25 µm result in a value of α of less than 1 µm. The SEM image also shows that the stencil remains intact after the metal deposition (Figure 2f). We further apply the same bridge concept to cantilevers having a width of 50 µm and a length of 900 µm. The results indicate that the 1 µm wide microbridges are capable of stabilizing the long and wide cantilevers (Figure S3, Supporting Information). We observe that the bridge connected at the end of the cantilever is broken after the metal deposition due to the accumulation of stresses by the added Cr layer. However, thanks to presence of other intact bridges, the value of α is less than 1 µm. Wider cantilevers can be better stabilized by connecting more bridges at the top of the structures. To sum up, without the application of microbridges, the fabricated cantilevers lead to significantly larger values of α on the deposited metal structures. The measured α can be up to 85 µm for the cantilever having a width of 50 µm and a length of 300 µm (Figure 2g). Whereas, by applying microbridges uniformly distributed across the cantilever structures, α is significantly reduced (Figure 2g). As expected, smaller values of α are observed with reduced interdistances between each bridge (i.e., more bridges in one cantilever) (Figure 2h). In the presented case, α can be reduced to less than 1 µm by having bridges placed at an interdistance of 25 µm across the 900 µm long cantilever. Moreover, we also investigate the limitations of the microbridge structure. Several microbridges with a width of 1 µm and lengths ranging from 80 to 500 µm are fabricated. The results show that bridges having a length of up to 500 µm are successfully fabricated without breaks (Figure S4, Supporting Information).

As a proof-of-concept for the bridge stencil approach proposed here, we demonstrate also a spiral structure, a geometry previously used as wireless heating elements for biomedical implants.[30] Microbridges with a width of 1 µm, which are uniformly distributed across the entire structure, force the suspended membrane to remain in the same plane as the surrounding membrane (**Figure 3**a). Continuous patterns are achieved by taking advantage of the blurring effect, where the line-of-sight evaporation process results in the material deposition
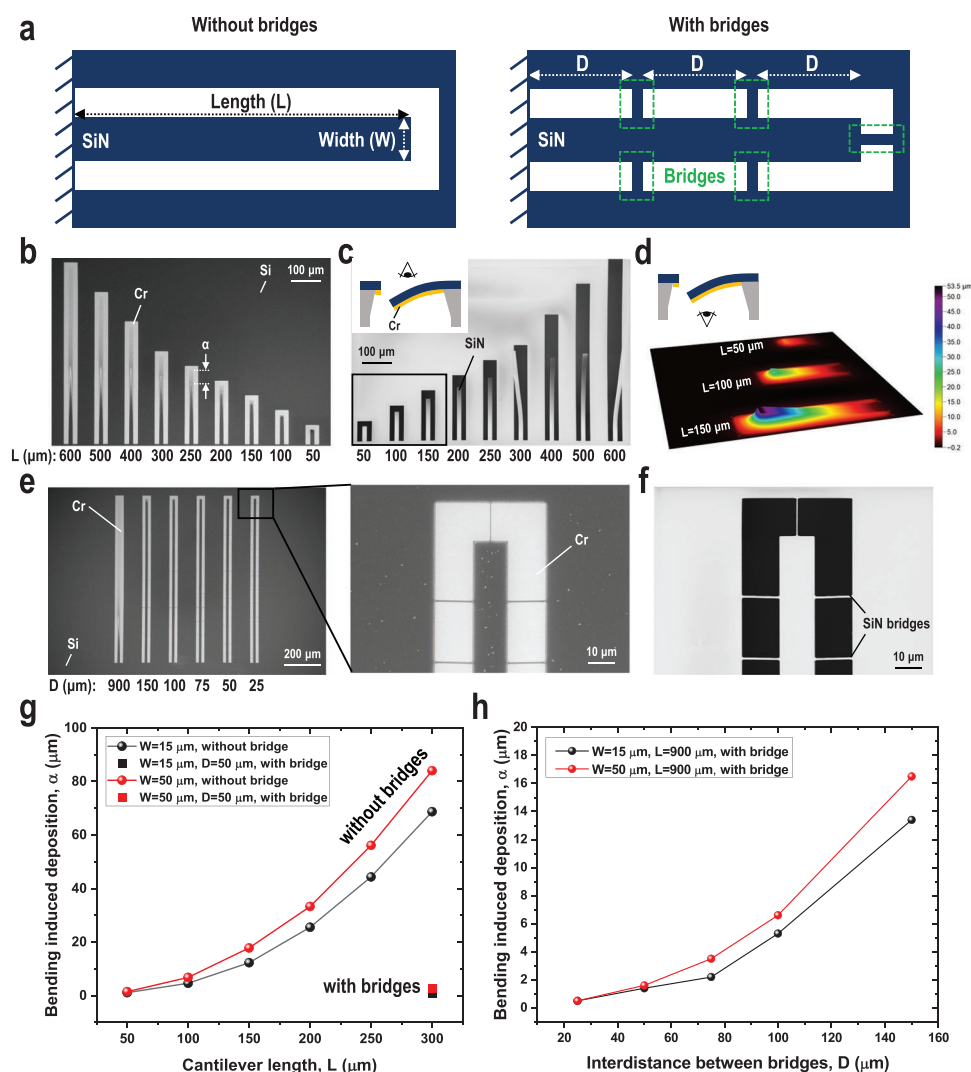
Figure 2. Detailed microbridge study with cantilever stencils. a) Schematic drawings showing the design of the cantilever stencils with and without bridges. The interdistance between the bridges is indicated with D. b,c) SEM images showing the deposition results of 25 nm Cr by cantilever stencils without bridges and the corresponding cantilever stencil images after metal deposition. The parameter α is defined as the length of the unwanted Cr structures deposited on a substrate due to the bending of the cantilevers. d) Confocal image showing the bending of the cantilever stencil after metal deposition. Insets in (c) and (d) show the schematic drawings of the structures and the direction from which the images are taken. e) SEM images showing the metal deposition results by microbridge cantilever stencils. The stencil contains cantilevers having a width of 15 μm and a length of 900 μm, supported by several bridges having different interdistances D. f) SEM image of the cantilever stencil having an interdistance of 25 μm between the bridges after metal deposition. g,h) Bending induced deposition length α without (g) and with microbridges (h). In (h), the length α is plotted as a function of the interdistances between the bridges D.

under the bridge shadow region when the stencil is placed at an appropriate distance from the substrate (Figure 3b). With the applied microbridges, stencils with spiral apertures are successfully fabricated and the confocal image show that the membrane bending induced by the intrinsic stress is less than 1.5 μm (Figure 3c,d). On the other hand, without microbridges, the membrane breaks during the release process (Figure S5, Supporting Information). The fabricated stencil is placed on a Si substrate and lifted above the substrate to a gap distance of 70 μm, which is introduced by inserting a Kapton tape in between, followed by the evaporation deposition of 5 nm Cr and 50 nm Au onto the substrate. Here, a 70 μm gap distance is chosen based on the calculated blurring length of 1.1 μm

(Equation (S1), Supporting Information). The resulting blurring length is large enough to fill the shadowed bridge area. Next, 5 nm Cr and 50 nm Au are evaporation deposited onto the substrate. The optical microscope images show that the designed spiral Cr/Au structure is successfully obtained (Figure 3e). The SEM images also show that the metals (Cr/Au) are deposited under the bridge area due to the blurring effect (Figure 3f). The measured width of the deposited structure without considering the halo of materials (i.e., the scattered particles induced by the surface diffusion of materials) is about 70 μm, which is in agreement with the calculated value (66 μm). To measure the deposition profile under the bridge region, AFM characterizations are performed. The results indicate a metal thickness of
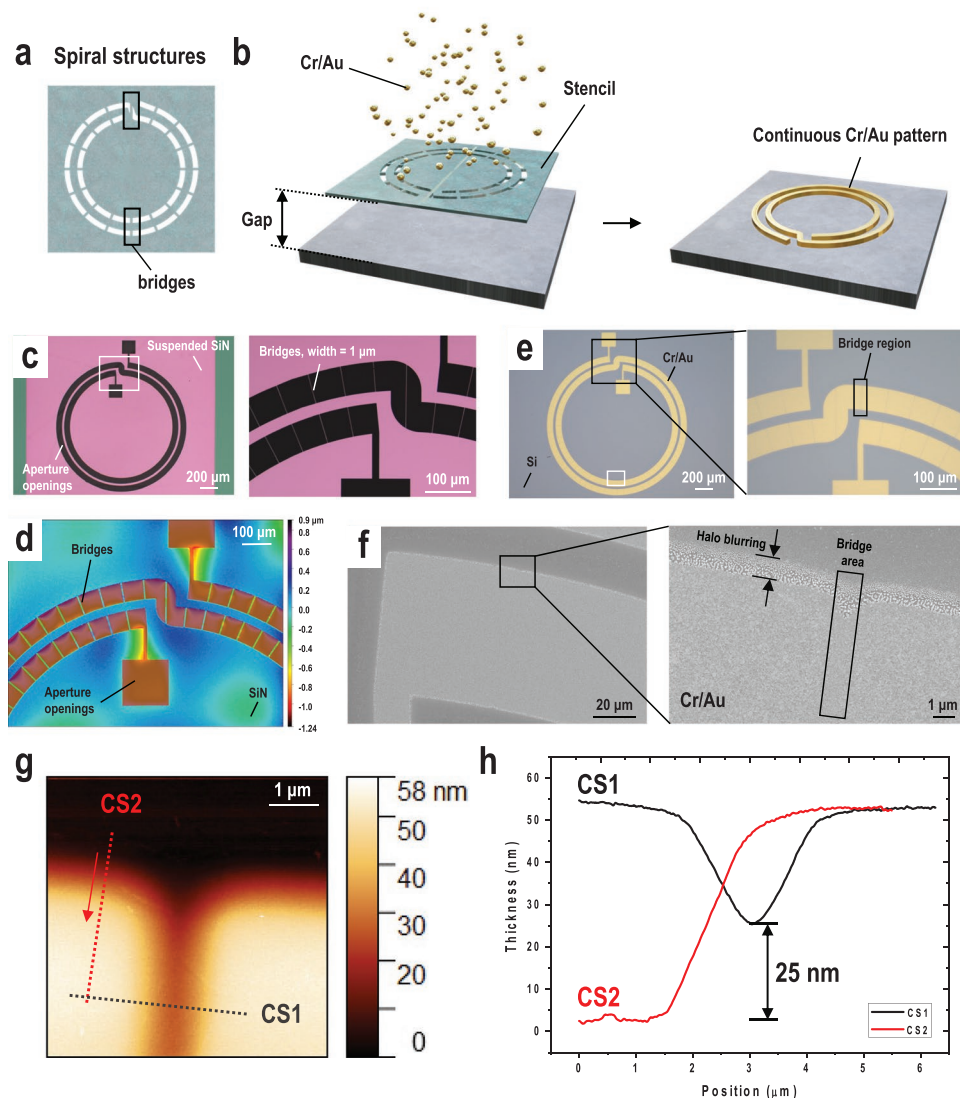
Figure 3. Bridge stencil applied to the fabrication of spiral structures. a) Schematic drawing illustrating the bridge stencil concept where several bridges are uniformly distributed on the suspended stencil membrane. b) Schematic drawings of the fabrication process. The stencil is lifted at a certain distance above the substrate, followed by evaporation deposition of Cr (5 nm)/ Au (50 nm) on the substrate. Thanks to the blurring effect, the resulting metallic spiral is continuous. c,d) Optical and confocal images of the SiN stencil after releasing. e,f) Optical and SEM images of the deposited Cr/Au structure on the Si substrate. The white rectangle shows where the AFM image is taken. g,h) AFM image and cross-section profile of the deposited structure along the dashed lines.

about 55 nm on the stencil aperture area and of about 25 nm under the shadowed bridge region (Figure 3g,h). The measured thickness of the metals deposited through the aperture openings agree well with the target thickness value. The thinner layer observed under the shadowed bridge region is in agreement with the reported literature[25] and it is obtained due to the smaller flux of atoms arriving under the bridge area.

To validate the use of the proposed bridge stencil approach on a variety of substrate materials, we apply the bridge stencils on a biodegradable poly lactic-*co*-glycolic acid (PLGA) substrate. In Section 2.2, we will discuss experiments performed also on polyimide (PI), poly(phthalaldehyde) (PPA), and parylene C. The stencil is attached to a PLGA substrate with a gap distance of 70 µm, followed by evaporation deposition of 5 nm Cr and

50 nm Au. The optical images reveal that the spiral structures are successfully fabricated on the PLGA substrate (**Figure 4**a). Next, we perform electrical measurements not only on the PLGA substrate, but also on a reference glass substrate to characterize the functionality of the deposited structures. The results show similar resistance values on both substrates with a value of 120 Ω (Figure 4b). The measured resistance values are within 15% deviation from the calculated values, assuming a gold resistivity of 0.036 Ω µm and a cross-section of 3.3 µm². The resistivity of gold is obtained by measuring the resistance values of gold structures fabricated on a reference SiN substrate using the four-point probe method. The width and the thickness of the deposited metal lines are obtained by an optical microscope and AFM, respectively. To demonstrate its applicability
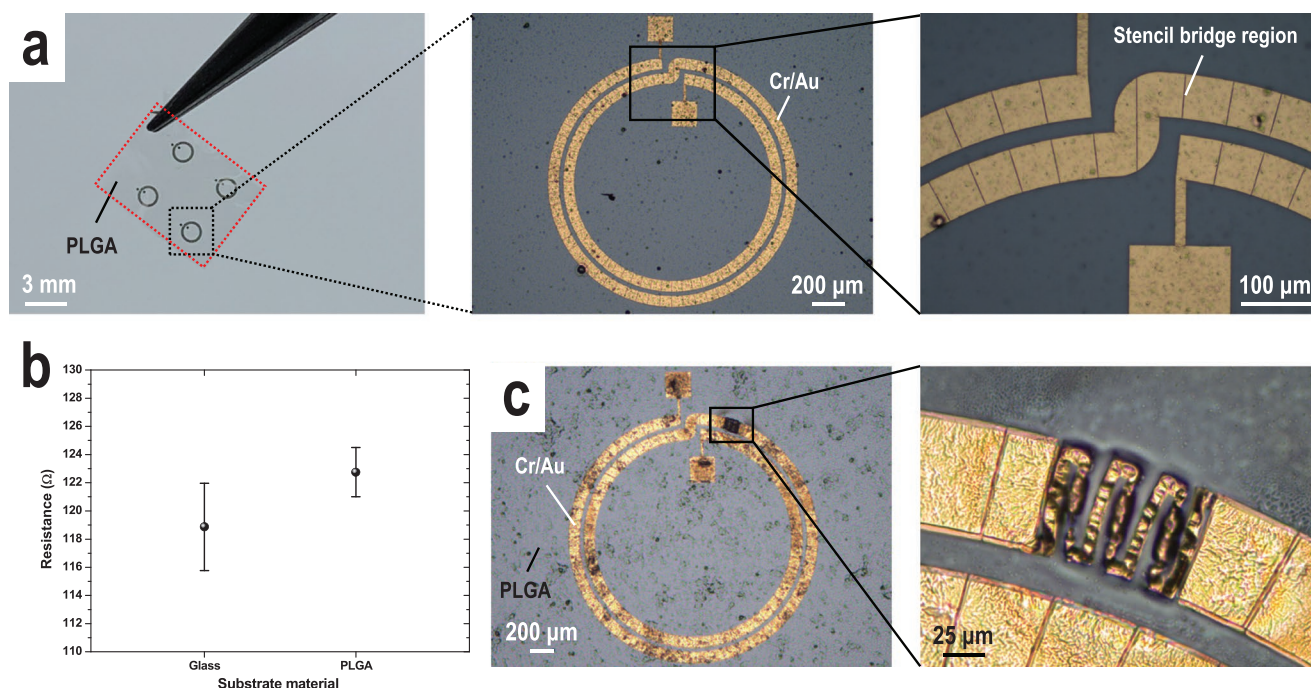
Figure 4. Fabrication results on a biodegradable PLGA substrate. a) Optical images showing the Cr/Au spiral structures on the biodegradable PLGA film. b) Resistance of the deposited structures on glass and PLGA substrates. Each data point contains measurement results from five nominally identical devices. The error bar represents the standard deviation. c) Optical images showing the fabricated spiral structure device after being electrically damaged by applying a voltage of 6.5 V.

as heaters for biomedical implants, a meandering structure is incorporated in the spiral design, which produces a local hot spot due to the increased current density in the meander.[30] As a demonstration, an increasing voltage is applied as heating source until electrical breakdown. It is observed that the device is burnt with an applied voltage of 6.5 V due to the damages in the incorporated meandering pattern (Figure 4c), which corresponds to a current density of 7.5×10^{10} A m^{-2}. The optical images reveal that the incorporated meandering structure and the underlying PLGA surface are damaged due to the increased temperature.

2.2. Nanobridge Stencil

To take a step further, we scale down the proposed bridge stencil concept to the sub-micrometer scale. A meandering pattern is demonstrated in this work as a proof-of-concept. The stencil used here is made of 100 nm-thick LS-SiN membranes supported by a Si frame and sub-micrometer scale apertures are defined by deep-ultraviolet (DUV) lithography. The rest of the fabrication process is identical to the one for microbridge stencils. The nanobridge stencil consists of meander apertures having a width of 350 nm and several 250 nm wide bridges uniformly distributed across the apertures. The membrane bending due to the intrinsic stress of the suspended SiN film is markedly reduced for the bridge stencil compared to the reference stencil without bridges (**Figure 5**a,c). The confocal images shows that the SiN membrane with nanobridges is nearly flat, whereas the one without bridges has a bending of

2.5 µm (Figure S6, Supporting Information). Additionally, in the highlighted region near the aperture openings, the bridge-supported stencil possesses a nearly flat membrane, whereas the one without bridge supports has a membrane bending of 0.5 µm, which would lead to an inaccurate pattern definition (Figure S6, Supporting Information). We then place the stencil in contact with a Si substrate, followed by evaporation deposition of 5 nm Cr and 50 nm Au. Using stencils without nanobridges, we observe irregular patterns due to the mechanical stress being built by the added metal layers, while the use of the nanobridge stencil allows obtaining well-defined patterns (Figure 5b,d). To elucidate the blurring induced pattern enlargement, we perform the deposition with three different gap distances (0, 25, and 50 µm) on a SiN substrate. The gap distances of 25 and 50 µm are created by inserting the Kapton tape with thicknesses of 25 and 50 µm between the stencil and the substrate. The SEM images indicate a width of the deposited metals of around 350, 650, and 950 nm for gap distances of 0, 25, and 50 µm, respectively (Figure S7, Supporting Information), which is within 20% deviation from the calculated blurring lengths (Equation (S1), Supporting Information). In addition, we observe a thickness reduction of the deposited metals not only under the bridges, but also in the regions under the aperture openings (Figure 5e–g). The AFM images reveal thickness reductions of around 35% (i.e., 35 nm instead of 55 nm) and 70% (i.e., 15 nm instead of 55 nm) for gap distances of 25 and 50 µm, respectively. Meanwhile, no thickness reduction is observed in the large aperture opening regions (i.e., a square electrical pad having a side of 80 µm; Figure S8, Supporting Information). This phenomenon is attributed to the
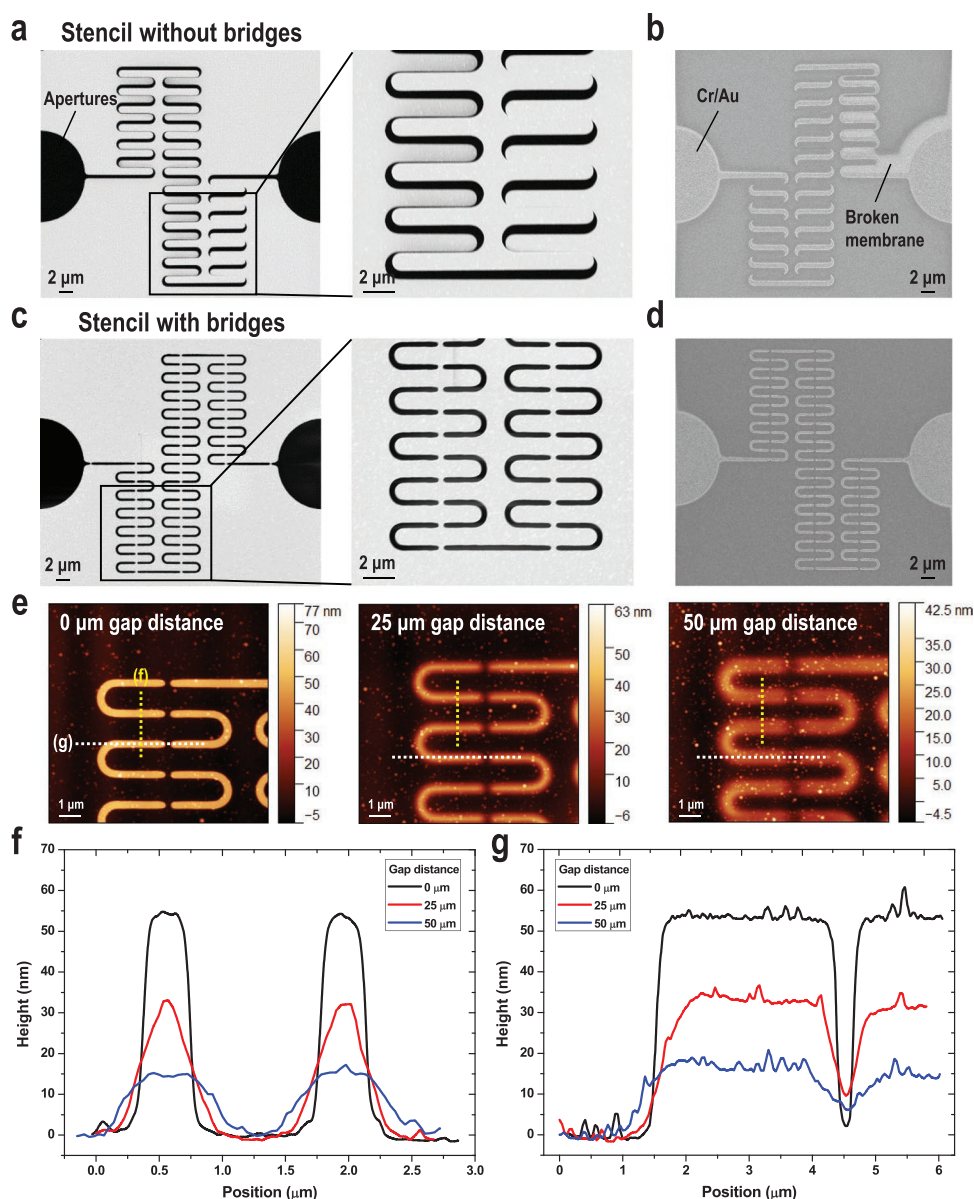
Figure 5. Nanobridge stencil with meandering pattern and the deposition results. SEM images showing the stencils a) without and c) with nanobridges and b,d) their corresponding Cr (5 nm)/Au (50 nm) deposition results on a Si substrate with zero gap distance. e) AFM images showing the meandering metal patterns deposited with gap distances of 0, 25, and 50 μm between the stencil and the substrate. The white and yellow lines indicate where the cross-section profiles are extracted. f,g) Cross-section profile of the Cr/Au structures deposited with different gap distances between the stencil and the substrate.

fact that when the stencil is lifted to a certain gap distance, it blocks a significant fraction of the incoming flux of atoms.[26] The different placement of stencils results in different effective source sizes, which influences the actual amount of atoms deposited on the substrate (Figure S9, Supporting Information). The reduced amount of atoms reaching the substrate is mainly affected by the stencil/substrate distance, the source/substrate distance, the source size and the aperture openings in the stencil. The reduction can be approximately estimated by calculating the effective source size $S' = \dfrac{A \times D}{G}$, where A is the stencil aperture opening size, D the substrate/source distance, and G the substrate/stencil gap. The equation is derived by considering the geometrical relation of the stencil and the line-of-sight trajectory of the evaporant. When the calculated effective source size is smaller than the evaporation source size, the substrate receives less atoms coming from the source, thereby leading to less material deposited on it. Based on the equation above, we obtain 25% and 80% of area reduction in the effective source size using $1 - \left(\dfrac{S'}{S}\right)^2$ for the cases of 25 and 50 μm gap distances, respectively. An accurate estimation of the thickness reduction remains challenging due to the difficulties in calculating the angular distribution of the evaporated atoms
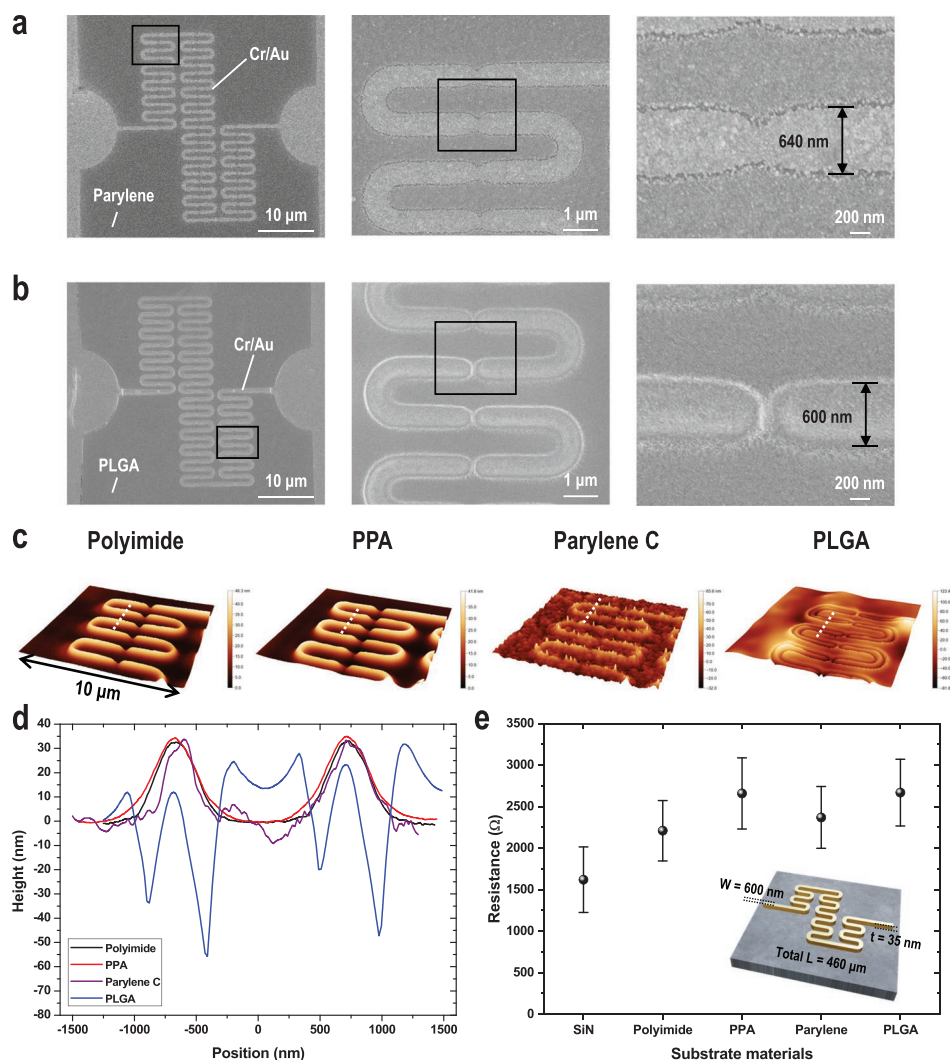
**ADVANCED
SCIENCE NEWS**

www.advancedsciencenews.com

**ADVANCED
MATERIALS
TECHNOLOGIES**

www.advmattechnol.de

Figure 6. Nanometer meandering patterns on a) biocompatible parylene and b) biodegradable PLGA substrates. c) AFM images showing the geometries of the fabricated metal structures. d) Cross-section profile of the metal structures along the white dashed lines in (c). e) Summary of measured electrical resistance values on different substrate materials. Each data point contains measurement results from at least ten samples. The error bar represents the standard deviation. Inset shows the schematic drawing of the meandering patterns and corresponding dimensions.

in the evaporation chamber. Furthermore, because the substrate is rotating during the evaporation deposition process to enhance the blurring effect, it makes this estimation even more challenging. Here, we aim at providing a rough estimation to explain the phenomenon of the observed thickness reduction. For the presented cases of 25 and 50 µm gap, the calculated effective source sizes are all smaller than the real source size of 16 000 µm. Therefore, the observed thickness reduction in both cases is in agreement with the proposed hypothesis. The measured resistance is infinite for a metal pattern produced with the stencil placed in contact with the substrate (zero gap) and therefore having an interrupted metal film, and 1600 and 1400 Ω for gap distances of 25 and 50 µm, respectively, where the blurring has created a conducting path under the bridge shadow. Based on the deposited metal geometries measured by SEM and AFM, the measured resistance values are 45% higher than the calculated values, assuming a gold resistivity of

0.036 Ω µm (Figure S10, Supporting Information). The deviation presumably comes from the inaccurate estimation of the deposited metal geometries under the bridges.

In the following, we apply the proposed nanobridge stencil on a wide range of substrate materials such as PI, parylene, PPA, and biodegradable PLGA to underline its potential for a large variety of applications. 5 nm Cr and 50 nm Au are evaporation-deposited on the polymer substrates with a fixed gap distance of 25 µm between the stencil and the substrate. The SEM images on the parylene and PLGA substrates clearly show that the metals are deposited not only under the stencil aperture regions, but also under the shadowed bridge region due to the blurring effect (**Figure 6**a,b). SEM images of the deposited structures on the other substrates are presented in Figure S11, Supporting Information. The fabricated meandering pattern having a line width of about 600 nm agrees well with the calculated blurring length. The AFM images show the geometries of

the deposited metal structures on different substrate materials (Figure 6c). On PI, PPA, and parylene substrates, meandering patterns are successfully produced as expected. The rougher geometry observed on the parylene substrate comes from the roughness of the parylene layer after it is chemical vapor deposited on a bare Si substrate (Figure S12, Supporting information). Interestingly, we notice a different behavior in the deposited metal structure on the PLGA substrate. The deposited metal is surrounded by a PLGA fence built during the evaporation deposition process. The cross-section view of the AFM images indicates that the deposited metals are inside the resulting PLGA channels (Figure 6d). We tentatively attribute the observed phenomenon to the low glass transition temperature (T_g) of PLGA, which was reported to be around 45 to 60 °C.[31] It has been widely studied that when a polymer is heated above its T_g, the polymer experiences reflow behavior due to the reduced viscosity.[32] With a local heating source, localized polymer reflow behavior was observed.[33] Furthermore, during the electron-beam evaporation deposition process, it was reported that the evaporated metal source heated the substrate material and induced a temperature increase on the substrate surface.[34] In the presented observation, the PLGA surface might experience local heating in the stencil aperture regions which results in polymer deformation during metal deposition. Last, the electrical characterization shows that similar resistance values are measured for all metal structures deposited on different polymeric substrate materials (Figure 6e). These results point out that the observed reflow behavior on the PLGA surface has no significant influence on the electrical characteristics of the deposited metal structures.

3. Conclusion

This work demonstrates a bridge stencil concept for the realization of arbitrarily shaped, continuous metallic patterns on various substrate materials. The suspended membrane is constrained to remain in the same plane as the surrounding membrane and frame by introducing uniformly distributed bridges across the stencil, which enables the realization of almost arbitrary aperture openings on the freestanding stencil membrane. Continuous metallic patterns are achieved by taking advantage of the blurring effect, obtained by introducing an appropriate gap between the stencil and the substrate. The effective stabilization of suspended stencil membranes by the integration of narrow bridges is characterized in detail by means of patterns deposited through stress-sensitive patterns having u-shapes, and compared to test patterns without bridge. Spiral structures at the micrometer scale are first produced on both rigid and soft biodegradable PLGA substrates. SEM and AFM results indicate that metallic spiral patterns are successfully fabricated. Electrical characterization results show similar resistance values among the used substrate materials. A potential application of the fabricated spiral structure as heaters for biomedical implants is demonstrated with a DC breakdown characterization. Furthermore, the bridge stencil is scaled down to the nanometer scale by utilizing DUV lithography. Geometrical and electrical characterization results show that meandering metallic patterns at the sub-micrometer scale are successfully

fabricated on a large variety of substrate materials, including biocompatible and biodegradable materials. The concept demonstrated here can be applied to realize almost arbitrary structure designs on a broad range of substrates, a crucial enabling step toward metal additive patterning on flexible and biodegradable material for implantable devices.

4. Experimental Section

Stencil Fabrication: A 500 nm thick low-stress SiN was first grown on both sides of a bare Si wafer by low pressure chemical vapor deposition (LPCVD). Next, 1 μm thick photoresist (AZ ECI 3007, Microchemicals GmbH) was spin-coated on the wafer, followed by defining the aperture openings with a direct laser writer. The SiN film is then etched by reactive ion etching (RIE) with a gas mixture of He, H_2, and C_4F_8. Then, oxygen plasma was performed to remove the photoresist. With the same method, a photolithography step was performed on the backside of the wafer but with a 5 μm thick photoresist (AZ ECI 3027, Microchemicals GmbH). Subsequently, the backside LS-SiN film was etched by RIE, followed by etching ≈400 μm Si bulk by the Bosch process. Last, KOH was used to etch the remaining Si and released the SiN membrane. At the end, the wafer was cleaved into 10 × 10 mm² chips. For the DUV stencil, the fabrication followed the same process but with a 100 nm thick LS-SiN. The aperture openings were defined by using a DUV stepper with a 450 nm thick photoresist (JSR M108Y, JSR Corp.), followed by etching the LS-SiN film and removing the resist. Backside opening of the wafer was defined by a direct laser writer with a 5 μm thick photoresist (AZ ECI 3027, Microchemicals GmbH). Then, RIE was performed to etch the backside LS-SiN film and the Bosch process to etch ≈200 μm Si bulk. Finally, the membrane was released by using KOH.

Polymer Film Fabrication: PI precursor (PI 2610, HD Microsystems) was spin-coated on a bare Si wafer to form a ≈5 μm thick PI film, followed by curing the film in an oven at 300 °C for 1 h. 5 μm thick Parylene layer was chemical vapor deposited on a bare Si wafer by using a commercial tool (Comelec C-30-S, Comelec SA). PPA (Allresist DE) solution (3 wt% in anisole) was spin-coated on a bare Si substrate, followed by baking at 90 °C for 3 min. 0.1 g PLGA particle was dissolved in 4 mL ethyl acetate and drop-casted on a Si wafer coated with a self-assembled trimethylsilyl chloride silane (Sigma-Aldrich) layer. Then, the solvent was evaporated in a fume hood at room temperature for at least 6 h to form a ≈7.5 μm thick PLGA film.

Supporting Information

Supporting Information is available from the Wiley Online Library or from the author.

Conflict of Interest

The authors declare no conflict of interest.

Data Availability Statement

The data that support the findings of this study are available from the corresponding author upon reasonable request.

[1] I. You, D. G. Mackanic, N. Matsuhisa, J. Kang, J. Kwon, L. Beker, J. Mun, W. Suh, T. Y. Kim, J. B.-H. Tok, Z. Bao, U. Jeong, *Science* **2020**, *370*, 961.

[2] X. Yu, Z. Xie, Y. Yu, J. Lee, A. Vazquez-Guardado, H. Luan, J. Ruban, X. Ning, A. Akhtar, D. Li, B. Ji, Y. Liu, R. Sun, J. Cao, Q. Huo, Y. Zhong, C. Lee, S. Kim, P. Gutruf, C. Zhang, Y. Xue, Q. Guo, A. Chempakasseril, P. Tian, W. Lu, J. Jeong, Y. Yu, J. Cornman, C. Tan, B. Kim, et al., *Nature* **2019**, *575*, 473.

[3] A. Petritz, E. Karner-Petritz, T. Uemura, P. Schäffner, T. Araki, B. Stadlober, T. Sekitani, *Nat. Commun.* **2021**, *12*, 2399.

[4] S.-K. Kang, R. K. J. Murphy, S.-W. Hwang, S. M. Lee, D. V. Harburg, N. A. Krueger, J. Shin, P. Gamble, H. Cheng, S. Yu, Z. Liu, J. G. McCall, M. Stephen, H. Ying, J. Kim, G. Park, R. C. Webb, C. H. Lee, S. Chung, D. S. Wie, A. D. Gujar, B. Vemulapalli, A. H. Kim, K.-M. Lee, J. Cheng, Y. Huang, S. H. Lee, P. V. Braun, W. Z. Ray, J. A. Rogers, *Nature* **2016**, *530*, 71.

[5] D.-H. Kim, J.-H. Ahn, W. M. Choi, H.-S. Kim, T.-H. Kim, J. Song, Y. Y. Huang, Z. Liu, C. Lu, J. A. Rogers, *Science* **2008**, *320*, 507.

[6] L. Tian, B. Zimmerman, A. Akhtar, K. J. Yu, M. Moore, J. Wu, R. J. Larsen, J. W. Lee, J. Li, Y. Liu, B. Metzger, S. Qu, X. Guo, K. E. Mathewson, J. A. Fan, J. Cornman, M. Fatina, Z. Xie, Y. Ma, J. Zhang, Y. Zhang, F. Dolcos, M. Fabiani, G. Gratton, T. Bretl, L. J. Hargrove, P. V. Braun, Y. Huang, J. A. Rogers, *Nat. Biomed. Eng.* **2019**, *3*, 194.

[7] J. Lee, H. R. Cho, G. D. Cha, H. Seo, S. Lee, C.-K. Park, J. W. Kim, S. Qiao, L. Wang, D. Kang, T. Kang, T. Ichikawa, J. Kim, H. Lee, W. Lee, S. Kim, S.-T. Lee, N. Lu, T. Hyeon, S. H. Choi, D.-H. Kim, *Nat. Commun.* **2019**, *10*, 5205.

[8] T.-H. Kim, K.-S. Cho, E. K. Lee, S. J. Lee, J. Chae, J. W. Kim, D. H. Kim, J.-Y. Kwon, G. Amaratunga, S. Y. Lee, B. L. Choi, Y. Kuk, J. M. Kim, K. Kim, *Nat. Photonics* **2011**, *5*, 176.

[9] K. Sim, S. Chen, Z. Li, Z. Rao, J. Liu, Y. Lu, S. Jang, F. Ershad, J. Chen, J. Xiao, C. Yu, *Nat. Electron.* **2019**, *2*, 471.

[10] S. Heo, J. Ha, S. J. Son, I. S. Choi, H. Lee, S. Oh, J. Jekal, M. H. Kang, G. J. Lee, H. H. Jung, J. Yea, T. Lee, Y. Lee, J.-W. Choi, S. Xu, J. H. Choi, J.-W. Jeong, Y. M. Song, J.-C. Rah, H. Keum, K.-I. Jang, *Sci. Adv.* **2021**, *7*, 28.

[11] O. Vazquez-Mena, L. Gross, S. Xie, L. Villanueva, J. Brugger, *Microelectron. Eng.* **2015**, *132*, 236.

[12] W. Wang, S. Wang, R. Rastak, Y. Ochiai, S. Niu, Y. Jiang, P. K. Arunachala, Y. Zheng, J. Xu, N. Matsuhisa, X. Yan, S.-K. Kwon, M. Miyakawa, Z. Zhang, R. Ning, A. M. Foudeh, Y. Yun, C. Linder, J. B.-H. Tok, Z. Bao, *Nat. Electron.* **2021**, *4*, 143.

[13] S.-W. Hwang, H. Tao, D.-H. Kim, H. Cheng, J.-K. Song, E. Rill, M. A. Brenckle, B. Panilaitis, S. M. Won, Y.-S. Kim, Y. M. Song, K. J. Yu, A. Ameen, R. Li, Y. Su, M. Yang, D. L. Kaplan, M. R. Zakin, M. J. Slepian, Y. Huang, F. G. Omenetto, J. A. Rogers, *Science* **2012**, *337*, 1640.

[14] W. Song, L. Kong, Q. Tao, Q. Liu, X. Yang, J. Li, H. Duan, X. Duan, L. Liao, Y. Liu, *Small* **2021**, *17*, 2101209.

[15] S. Aksu, M. Huang, A. Artar, A. A. Yanik, S. Selvarasah, M. R. Dokmeci, H. Altug, *Adv. Mater.* **2011**, *23*, 4422.

[16] O. Vazquez-Mena, T. Sannomiya, M. Tosun, L. G. Villanueva, V. Savu, J. Voros, J. Brugger, *ACS Nano* **2012**, *6*, 5474.

[17] O. Vazquez-Mena, G. Villanueva, V. Savu, K. Sidler, M. A. F. van den Boogaart, J. Brugger, *Nano Lett.* **2008**, *8*, 3675.

[18] P. Schüffelgen, D. Rosenbach, C. Li, T. W. Schmitt, M. Schleenvoigt, A. R. Jalil, S. Schmitt, J. Kölzer, M. Wang, B. Bennemann, U. Parlak, L. Kibkalo, S. Trellenkamp, T. Grap, D. Meertens, M. Luysberg, G. Mussler, E. Berenschot, N. Tas, A. A. Golubov, A. Brinkman, T. Schäpers, D. Grützmacher, *Nat. Nanotechnol.* **2019**, *14*, 825.

[19] R. Lüthi, R. R. Schlittler, J. Brugger, P. Vettiger, M. E. Welland, J. K. Gimzewski, *Appl. Phys. Lett.* **1999**, *75*, 1314.

[20] V. Savu, M. A. F. van den Boogaart, J. Brugger, J. Arcamone, M. Sansa, F. Perez-Murano, *J. Vac. Sci. Technol., B: Microelectron. Nanometer Struct.–Process., Meas., Phenom.* **2008**, *26*, 2054.

[21] S. Kuiper, C. van Rijn, W. Nijdam, M. Elwenspoek, *J. Membr. Sci.* **1998**, *150*, 1.

[22] M. A. F. van den Boogaart, L. M. Doeswijk, J. Brugger, *J. Microelectromech. Syst.* **2006**, *15*, 1663.

[23] M. A. van den Boogaart, M. Lishchynska, L. M. Doeswijk, J. C. Greer, J. Brugger, *Sens. Actuators, A* **2006**, *130–131*, 568.

[24] O. Vazquez-Mena, K. Sidler, V. Savu, C. W. Park, L. Guillermo Villanueva, J. Brugger, *IEEE Trans. Nanotechnol.* **2011**, *10*, 352.

[25] A. Tixier, Y. Mita, J. P. Gouy, H. Fujita, *J. Micromech. Microeng.* **2000**, *10*, 157.

[26] O. Vazquez-Mena, L. G. Villanueva, V. Savu, K. Sidler, P. Langlet, J. Brugger, *Nanotechnology* **2009**, *20*, 415303.

[27] Z. Racz, A. Seabaugh, *J. Vac. Sci. Technol., B: Microelectron. Nanometer Struct.–Process., Meas., Phenom.* **2007**, *25*, 857.

[28] P. Fesenko, V. Flauraud, S. Xie, J. Brugger, J. Genoe, P. Heremans, C. Rolin, *Cryst. Growth Des.* **2016**, *16*, 4694.

[29] P. Fesenko, V. Flauraud, S. Xie, E. Kang, T. Uemura, J. Brugger, J. Genoe, P. Heremans, C. Rolin, *ACS Appl. Mater. Interfaces* **2017**, *9*, 23314.

[30] M. Rüegg, R. Blum, G. Boero, J. Brugger, *Adv. Funct. Mater.* **2019**, *29*, 1903051.

[31] D. N. Kapoor, A. Bhatia, R. Kaur, R. Sharma, G. Kaur, S. Dhawan, *Ther. Delivery* **2015**, *6*, 41.

[32] H. Schift, C. Spreu, A. Schleunitz, J. Lee, *Microelectron. Eng.* **2011**, *88*, 87.

[33] C. Dai, K. Agarwal, J.-H. Cho, *ACS Nano* **2018**, *12*, 10251.

[34] N. Bowden, S. Brittain, A. G. Evans, J. W. Hutchinson, G. M. Whitesides, *Nature* **1998**, *393*, 146.